J Therm Spray Tech (2019) 28:1379–1401
https://doi.org/10.1007/s11666-019-00918-5

PEER REVIEWED

Development and Characterization of High-Velocity Flame Sprayed Ni/TiO_2/Al_2O_3 Coatings on Hydro Turbine Steel

Vibhu Sharma[1] · **Manpreet Kaur**[2] · **Sanjeev Bhandari**[2]

Submitted: 2 May 2019 / in revised form: 10 September 2019 / Published online: 20 September 2019

Abstract Nickel-based coatings deposited by high-velocity flame spray (HVFS) process have been widely used to overcome the slurry erosion in a hydro turbine, where many turbine components are subjected to severe erosion failure. In this work, new kind of multi-dimensional Ni-40TiO_2 and Ni-20TiO_2-20Al_2O_3 coatings consisting of nanostructured and micron-sized particles of TiO_2 and Al_2O_3 were developed by HVFS process on CA6NM(13Cr4Ni) turbine steel. The in-depth characterization of the synthesized nanostructured powders, prepared coating compositions and the deposited coating was done through dynamic light scattering, scanning electron microscopy, energy-dispersive spectroscopy and x-ray diffraction techniques. The mechanical and microstructural properties of the as-sprayed specimens were evaluated and discussed in this paper. The results showed that the multi-dimensional Ni-40TiO_2 coating possessed lower porosity (0.8-2.0%), higher avg. microhardness (605 ± 37 $HV_{0.1}$), and better bond strength (66.4 MPa) than the Ni-20TiO_2-20Al_2O_3 coating.

Keywords characterization · HVFS · hydro turbine steel · nanostructured coatings · SEM

✉ Manpreet Kaur
manpreet.arora@bbsbec.ac.in

Vibhu Sharma
vibhu_24@hotmail.com

[1] I.K. Gujral Punjab Technical University, Jalandhar, India

[2] Baba Banda Singh Bahadur Engineering College, Fatehgarh Sahib, India

Introduction

Erosion is a major issue in submerged parts of the hydro turbine, which radically abbreviates the life expectancy of the turbine components and decreases the general effectiveness of hydropower ventures (Ref 1, 2). The turbines indicate declined effectiveness following a couple of long span of work as they get seriously harmed because of different problems. Erosion results in the alteration of blade profile, increased vibration, fatigue damage, inefficient operation and system failure in the hydro turbines. This problem is a major concern in the case of small hydropower plants, as most of these plants are run-of-river schemes and are situated in steep hilly terrains. During the rainy season, a large amount of sediments (as high as 20,000 ppm) are present in water and it becomes difficult to remove all these sediments before passing through the turbine (Ref 3). Erosion of hydropower plants may result in substantial loss of revenues.

CA6NM steel is a common material for hydro turbines because of its good corrosion and cavitation resistance and high impact toughness (Ref 4). The steel has always remained a preferred choice by various industries as it can be used as hydro turbine blade material, pump material, compressors and valves. However, steel lacks slurry erosion resistance. Therefore, it becomes necessary to study and understand the performance of this steel in slurry erosion conditions. Among the different preventive measures, surface coatings offer a method for expanding the edge of the utilization of materials at the upper end of their performance capacities, by keeping up the mechanical, physical properties and shielding the components from wear and erosion. It has been observed that among different coating compositions investigated in the literature, WC-based coatings have been widely investigated. Literature

Table 1 Details of powders used for synthesizing the nanostructured powder

Powder	Size	Make	Morphology
Titania (TiO_2)	40 ± 10 μm	Sigma-Aldrich	Irregular
Alumina (Al_2O_3)	40 ± 10 μm	Sigma-Aldrich	Irregular and angular

Table 2 Milling parameters used to synthesize the nanostructured TiO_2 and Al_2O_3 powders

Mill details	Milling parameters
Vessel capacity: 25 mL	Milling atmosphere: vacuum
Milling Media: tungsten-carbide balls	Balls-to-powder weight ratio: 10:1
Mill material: tungsten carbide	Milling speed: 450 rpm for TiO_2 and 600 rpm for Al_2O_3
PCA: stearic acid and ethanol	Amount of PCA (wt%): 1.5-2.0%
	Milling time: 30 h for TiO_2 and 40 h for Al_2O_3
	Initial powder: 20 g

Table 3 Composition of uncoated substrate steel

C	Si	Mn	Ni	Cr	Mo	Fe
0.82 ± 0.03	0.66 ± 0.05	1.05 ± 0.11	3.25 ± 0.19	13.83 ± 0.20	0.43 ± 0.09	Balance

studies revealed that slurry erosion aspects of hydro turbine steel have not yet been studied in sufficient detail. Less coating compositions have been explored in the field of slurry erosion testing of thermal-spray-coated hydro turbine steel, whereas the losses due to these degradation mechanisms are tremendous. One of the thermal spray coating technique that is the high-velocity flame spray (HVFS) process presents a versatile approach and is a suitable candidate for the deposition of nanostructured composite coatings in terms of materials, deposition medium and thickness compared to other deposition processes (Ref 5-7). The developed coatings are much thicker than those achievable by other methods. Moreover, for increasing the performance of the steel against the slurry erosion there is a need to explore the performance of ceramic materials like alumina (Al_2O_3), titania (TiO_2), zirconia (ZrO_2) and silicon oxide (SiO_2). These materials are being used as reinforcements in other materials to prepare thermal spray composite coating compositions (Ref 8, 9). Further, the deposition of alumina and titania composites by the thermal spray techniques has been given less attention in spite of their excellent properties such as higher hardness, higher wear, corrosion resistance and good wettability (Ref 10). Moreover, the limited literature is available showing the mechanical blending of nickel with alumina and/or titania nanostructured powders (Ref 7, 9).

Ni is a transition metal which is ductile. In addition, it has a high bonding strength and provides resistance to abrasion and erosion wear if used with ceramics (Ref 11, 12). Ni has been selected as the candidate material for matrix because of its better fracture toughness than Al and Ti and economical as compared to Cr or Co. Alumina (Al_2O_3) generally refers to corundum. It is a white oxide that exists in several phases as gamma, delta, theta and alpha. Both the alumina and titania powders possess many properties like high hardness, low coefficient of friction, high stability, high insulation, good wear properties and transparency (Ref 13). These are being used as the catalysts, insulators, surface protective coatings and in the composite materials (Ref 14, 15). Parida et al. (Ref 16) investigated the behavior of Ni-TiO_2 coating and reported that the mechanical properties of the coatings were highly dependent upon the grain boundary/particle size of the coating powders. Benea et al. (Ref 17) developed the Ni-Al_2O_3-TiO_2 composite coatings for automobile, medical, textile and printing applications. The authors reported the better performance of the coatings against wear applications. Kim et al. (Ref 18) investigated the performance of TiO_2 nanostructured coatings for stainless steel. The coatings were smooth without the presence of cracks and showed excellent erosion resistance. Yang et al. (Ref 19) developed the Al_2O_3-TiO_2-ZrO_2 nanocomposite coatings on carbon steel by a plasma spray technique. The authors enunciated that the formulation of nanostructured coating possessed higher hardness and toughness compared with the conventional micron-structured coatings. Grewal et al. (Ref 6) and Kumar et al. (Ref 7, 9) investigated the slurry erosion behavior of Ni/Al_2O_3 and Ni/TiO_2/Al_2O_3 coating developed on the CA6NM steel turbine steel. The authors prepared the coating composition by using micron-sized particles and proposed the best coating composition for the

Table 4 Details of coating feedstock material used for coating

Powder	Make	Size	Particle shape
Nickel	Jayesh Industries (Mumbai)	45 ± 10 μm	Spherical
Titania (TiO_2)	Sigma-Aldrich Chemicals Limited, Germany	40 ± 10 μm	Irregular
Titania (TiO_2)	Synthesized in the laboratory	185 ± 5 nm	Agglomerate angular
Alumina (Al_2O_3)	Sigma-Aldrich Chemicals Limited, Germany	40 ± 10 μm	Angular and blocky
Alumina (Al_2O_3)	Synthesized in the laboratory	216 ± 5 nm	Agglomerate angular

Table 5 Designation and percentage proportion of coating elements

Designation	Elements				
	Nickel, μm	Titania, μm + nm		Alumina, μm + nm	
Ni-40TiO_2	60%	35%	5%	…	…
Ni-20TiO_2-20Al_2O_3	60%	15%	5%	15%	5%

Table 6 List of parameters used in HVFS process for coating deposition

Parameter	O_2 pressure, kg/cm^2	Acetylene pressure, kg/cm^2	O_2 flow rate, SCFH	Acetylene flow rate, SCFH	Working distance, mm	Air carrier gas flow, SCFH	Powder feed rate, g/min
Value	2.5	1.1	50	46-47	200	10-12	10

SCFH standard cubic feet per minute

Table 7 Mechanical properties of the as-sprayed coatings

Specimen	Coating thickness, μm	Avg. microhardness HV	Avg surface roughness Ra, μm	Avg. coating density, kg/m^3	Bond strength, MPa	Porosity, %	Fracture toughness, MPa-m$^{1/2}$
Ni-40TiO_2	422 ± 10	605 ± 37	6.61 ± 0.4	6100 ± 60	66.4	0.8-2.0	1.8 ± 0.2
Ni-20TiO_2-20Al_2O_3	354 ± 10	585 ± 33	9.39 ± 0.4	5910 ± 80	61.7	1.6-3.6	1.6 ± 0.2

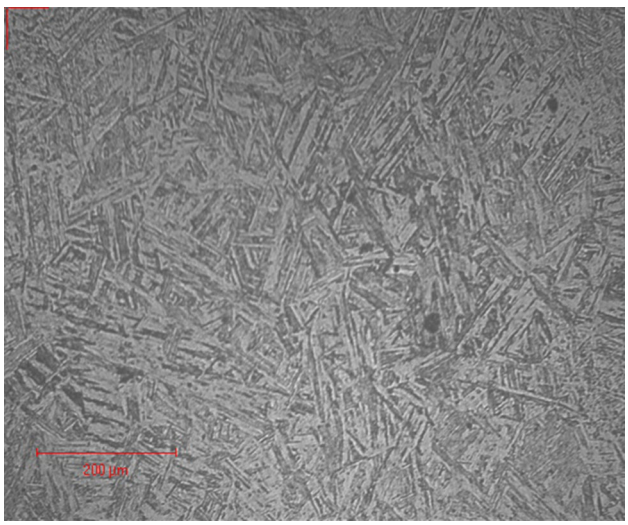

Fig. 1 Optical micrograph of CA6NM steel

mitigation of erosion problem. However, there is a need to describe the effect of nanostructured particles added as the reinforcement materials in the nickel matrix. Therefore, the literature studies motivated the authors to study the effect of nanostructured Al_2O_3 and TiO_2 powders added as the reinforced materials in the nickel-based matrix.

In the present study, the work was started with the synthesis of nanostructured titania powder (TiO_2) and nanostructured alumina powder (Al_2O_3). The nanostructured powders were further reinforced in the pure nickel powder matrix. The powders were mixed in different proportions. The aim of this work was to develop novel kind of multi-dimensional Ni-40TiO_2 and Ni-20TiO_2-20Al_2O_3 composite coatings containing nanostructured and micron-sized particles of TiO_2 and Al_2O_3 deposited by the HVFS process. The designed compositions of the coatings were expected to improve the mechanical properties such as microhardness, porosity, bond strength and toughness in

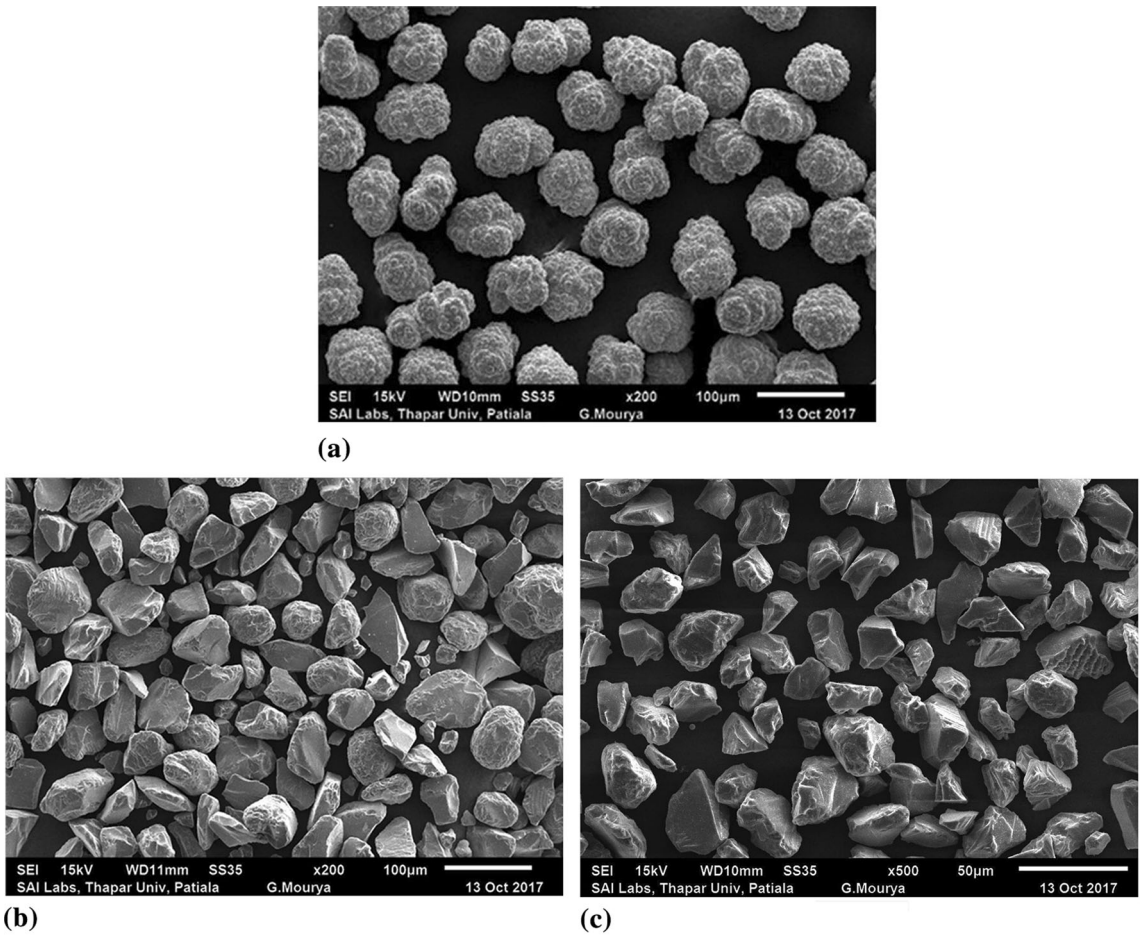

Fig. 2 SEM micrograph of as-received (a) Ni powder, (b) TiO_2 and (c) Al_2O_3 powders

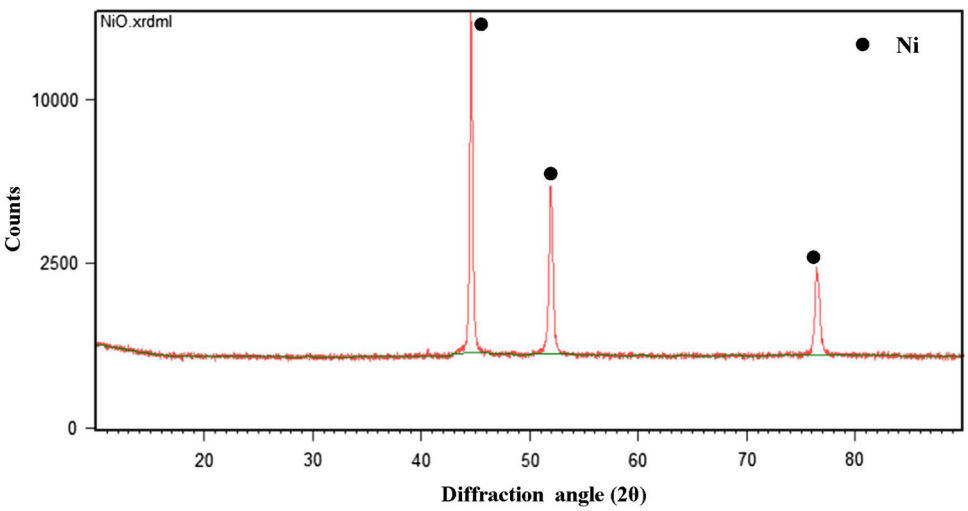

Fig. 3 X-ray diffraction analysis of as-received Ni powder

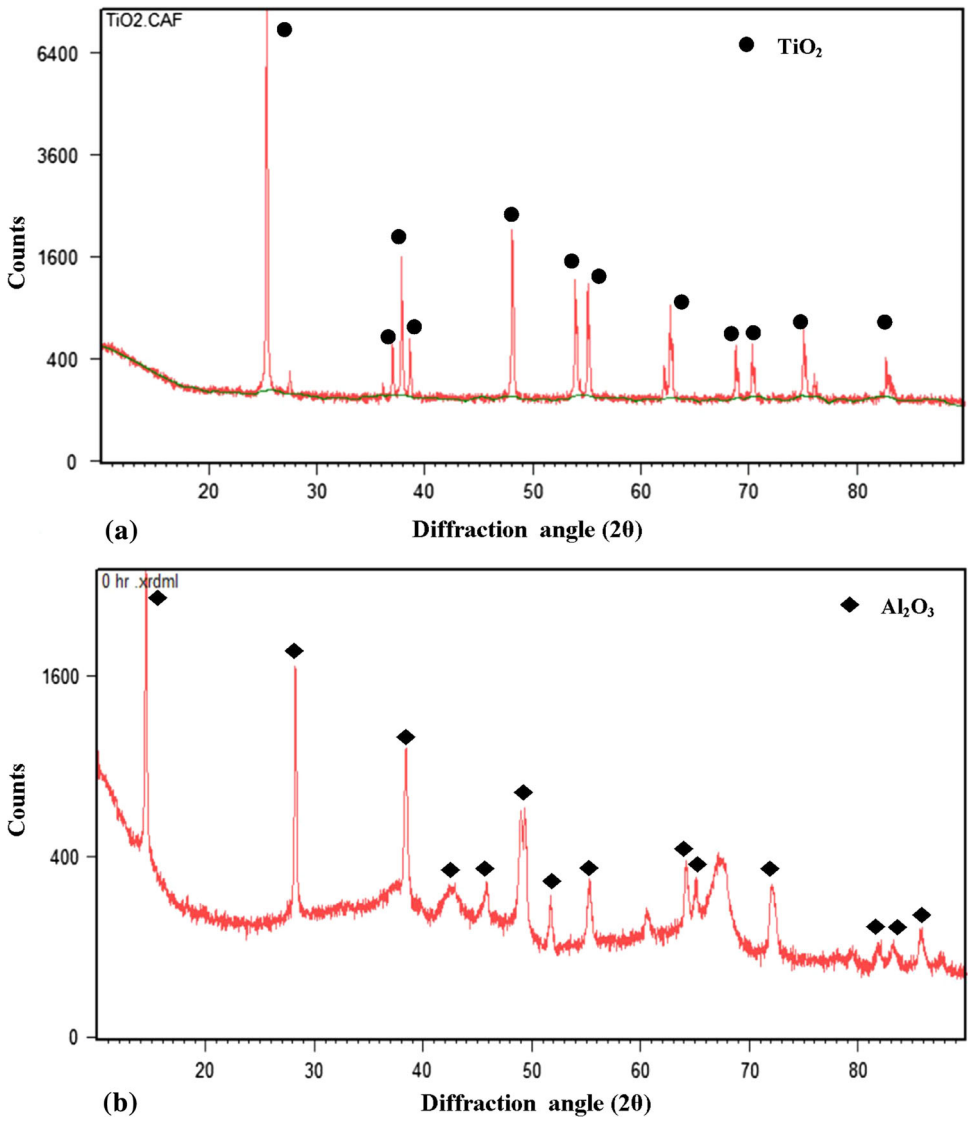

Fig. 4 X-ray diffraction analysis of as-received (a) TiO_2 and (b) Al_2O_3 powders

the coating from that obtained in the previous studies (Ref 7, 9).

Experimental Procedure

Synthesis of Nanostructured TiO_2 and Al_2O_3 Powder

The titania and alumina nanostructured particles were synthesized on the laboratory scale by attrition milling of micron-size powders under vacuum conditions, details of which are presented in Table 1. The synthesis of nanostructured titania and alumina powders was done separately by the high-speed planetary ball milling machine PM100 from RETSCH. The titania and alumina powders were milled for a period of 30 and 40 h, respectively. Table 2 shows the details of the milling parameters used in the present investigation. To start with, the jar rotates for 6 min in the clockwise direction. The pause of 3 min was given for lesser heat generation that might happen during the milling process. Again the jar rotates at the prescribed time in an anticlockwise direction. This is the characteristic feature of the ball milling machine. The particle size of the prepared powders and its percentage distribution were determined by the dynamic light scattering (DLS) analysis.

Coating Substrate and its Preparation

In the present investigation, the substrate steel selected for the study was a hydro turbine material, namely CA6NM steel. The material was procured from the Mithila

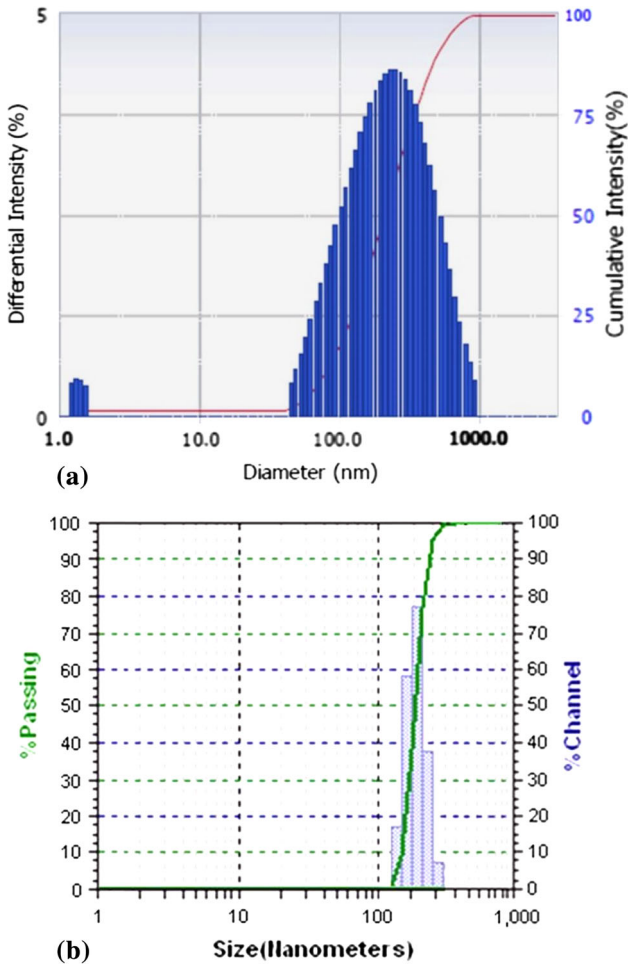

Fig. 5 Particle size distribution analysis of ball-milled powder of (a) TiO_2 after 18 h (b) Al_2O_3 after 30 h

Malleables Pvt. Ltd., Sirhind (Punjab, India). The industry is involved in manufacturing different steel materials required in hydropower plants. The composition of the steel is presented in Table 3. The sample size of 20 mm × 20 mm × 5 mm has been cut from the turbine steel bar for the slurry erosion tests. Prior to the coating deposition, the steel specimens were polished with emery papers embedded with SiC particles lower to 180 grit size. Afterward, the surfaces of the specimens were shot-blasted by abrasive alumina particles of grit size 20 µm for achieving the rough surface. The average value of surface roughness obtained before the coating was 8 to 11 µm as recorded with the surface roughness tester (Make: Mitutoyo, Japan Model: SJ301) available at MECPL, Jodhpur. The instrument was having a least count of 0.1 µm with sampling length as 4 mm.

Formulation of Coating Feedstock Powder

The coating powders used in this study were commercially available pure nickel (Ni) powder, titanium oxide (TiO_2) powder, alumina (Al_2O_3) powder and synthesized nanostructured TiO_2 and Al_2O_3 powders. Table 4 presents the details of powders used as a feedstock material. The Ni-40TiO_2 powder was mixed in the ratio 60:40 by weight, and Ni-20TiO_2-20Al_2O_3 powder was mixed in the ratio 60:20:20 by weight. The details of the coating compositions and designations are presented in Table 5.

Coating Deposition

The prepared coating powders were deposited on to the selected substrate material at MECPL (Metallizing Equipment Company Pvt. Ltd.), Jodhpur, Rajasthan, India, using a 6P jet gun by HVFS process. Table 6 presents the parameters set during the deposition of the coating by the HVFS process. The air was used as a carrier gas type. The gun traverse speed and crossover speed used were 0.25 and 0.25 m/s. The speed of powder disk was set in the range of 5 rpm.

Characterization of Substrate, Synthesized Nanostructured Powders and As-Sprayed Coatings

An optical microscope (OM) was used for the microstructural examination of the CA6NM steel surface. The cut specimens of uncoated steel were polished on a machine having 180-grit emery belts. Further, it was polished manually up to 2000 grits using SiC emery papers. Finally, the polishing was completed on the disk polishing machine wrapped with soft nylon cloth using levigated alumina paste of 1 µm size. The polished specimens were then etched with 87 Glyceregia (15 cc HCl + 10 cc HNO_3 + 5 cc glycerin) prepared according to the ASTM-407 standard. The prepared specimens were examined under inverted optical microscope provisioned with imaging software Envision 3.0. XRD analysis of the prepared nanostructured powders, micron-size powders, two composite powders and the as-sprayed coated specimens was performed to identify the different existing elements/phases in the synthesized powders and the coatings. The analysis was done by using an X'pert High score Pro (Model: Expert Pro MPD, Make: PAN analytical, Netherland) with CuKα radiation in the 2θ range from 20° to 90°. Various phases in the prepared composition were identified using software X'pert High Score Pro software, and accordingly, graphs were recorded.

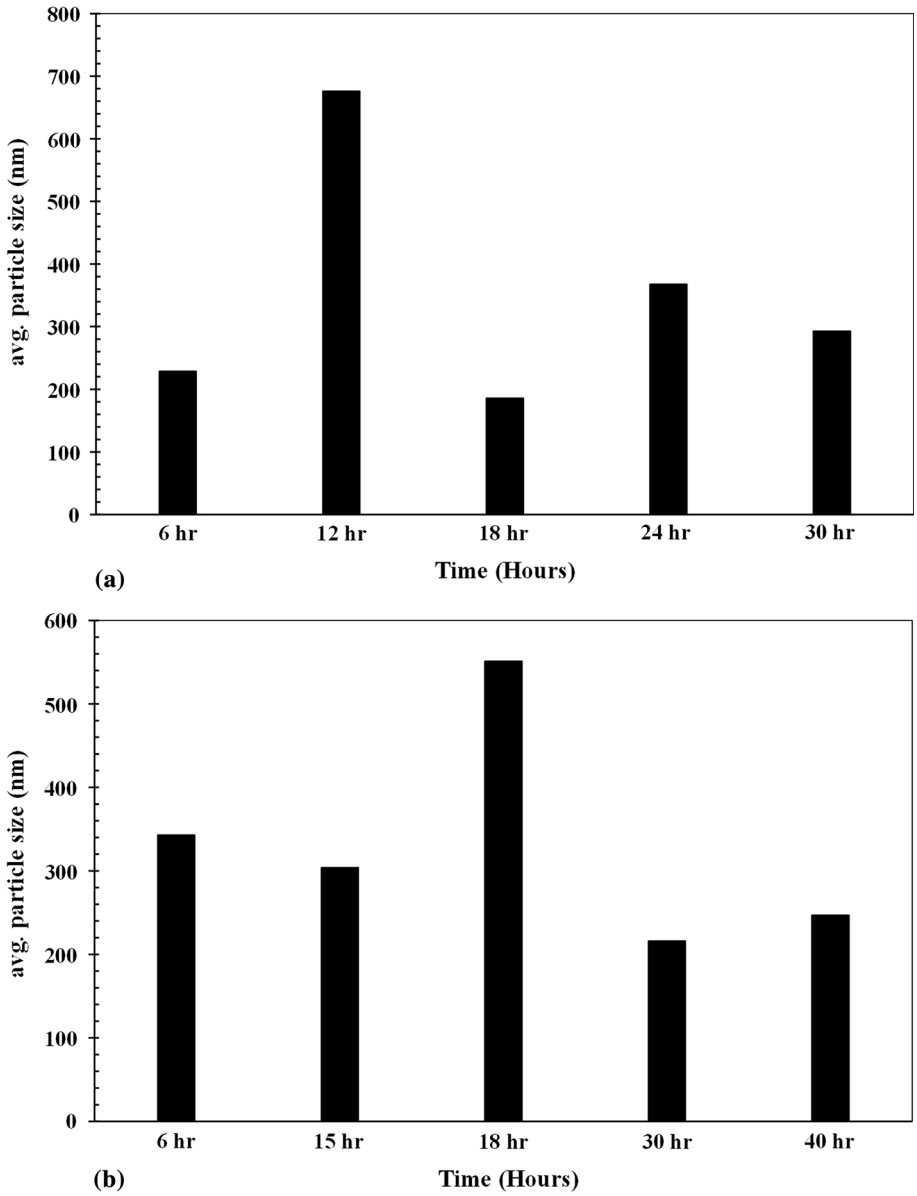

Fig. 6 Particle size (nm) verses milling time (in hours): (a) TiO_2 and (b) Al_2O_3 nanostructured powders synthesized after different hours

Further, the surface morphology of the prepared nanostructured powders, micron-size powders, two composite powders and the as-sprayed specimens was examined by using SEM (scanning electron microscope), (Make: JEOL, USA Model: JSM-6610LV) and the EDS (equipped with energy-dispersive spectroscopy) analysis to know the elements in the prepared powders and in the as-sprayed coatings. For the analysis of cross-sectional morphology, the as-sprayed specimens were cut with a low-speed diamond cutter (Make: Chennai Metco Private Limited, Chennai, India, and Model: BAINCUT-LSS). Afterward, the cut specimens were mounted in transoptic epoxy resins by the hot mounted hydraulic mounting press (Model: BAINMOUNT-H from Chennai Metco Private Limited, Chennai, India) so as to examine the details of the cross section. Afterward, the mounted specimens were mirror-polished using various sizes of emery papers and by rotating on the disk polishing machine with 1-μm levigated alumina paste. Specimens were then completely washed and dried before being examined. The fracture toughness of the coating was estimated by using (Eq 1), and density of the coating was estimated by using (Eq 2):

$$Kc = 0.079\left(\frac{p}{a}\right)^{\frac{3}{2}}\log\left(4.5\frac{a}{c}\right) \quad \text{(Eq 1)}$$

where 'p' is the indented load in mN, 'c' is the indentation half diagonal (μm), and 'a' is crack length measured from indentation center (μm). This analysis was carried out at Indian Institute of Technology (IIT) Ropar, Punjab, India:

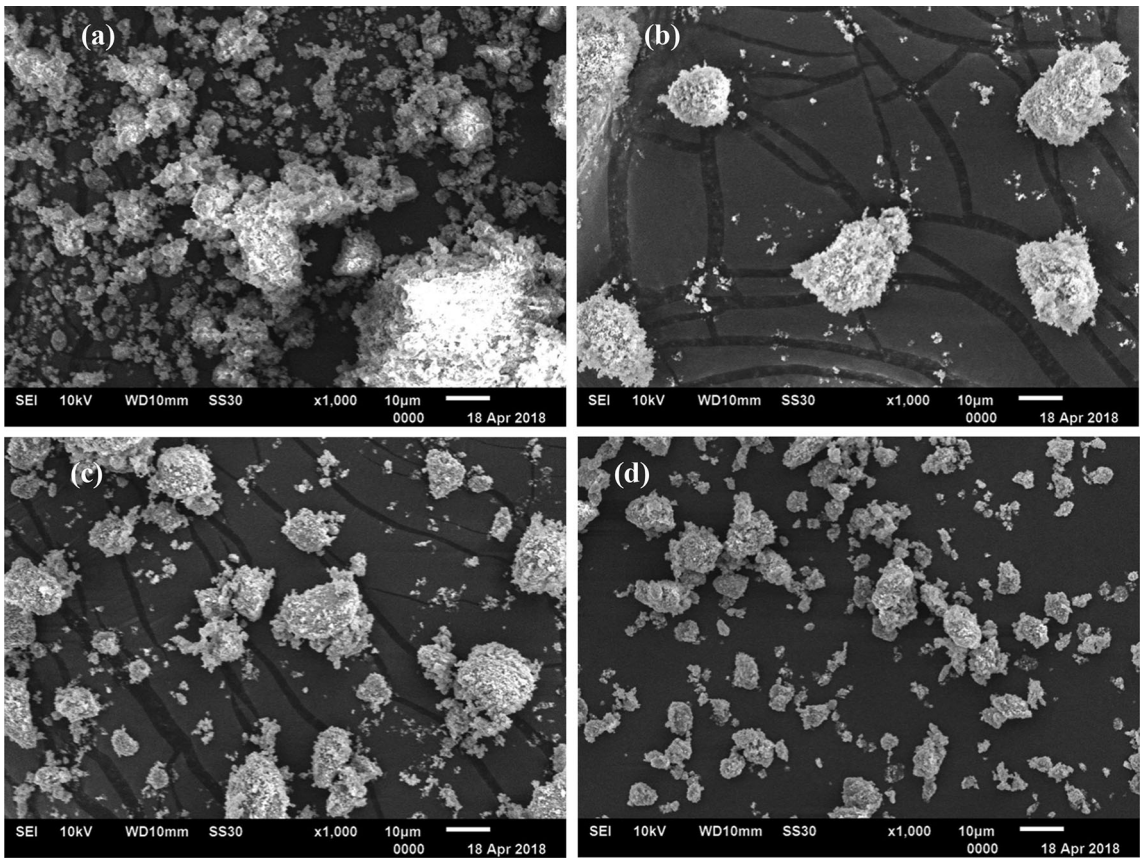

Fig. 7 SEM micrograph of synthesized TiO_2 powder ball-milled after (a) 12 h (b) 18 h (c) 24 h and (d) 30 h

$$\text{Coating density } (\rho)\ \text{g/cm}^3 = \rho_1\left(\frac{m_1}{m_a - m_1}\right) \qquad \text{(Eq 2)}$$

where ρ_1 is the density of water (1 g/cm^3) at room temperature, m_a is the weight of the coating in the air (g), and m_1 is the weight of coating in water (g). The coating density was calculated by using Archimedes principle. m_1 was estimated by firstly measuring the weight of the coated specimen in the beaker of water, and then, the coating was carefully removed from the specimen with the help of emery paper. Afterward, the weight of the specimen was again measured in the same beaker of water. The difference between the two values gave the mass of the coating in water. Similarly, m_a was calculated by measuring the weight of coated and the uncoated specimens in air. The difference between the two values gave the mass of the coating in air.

The coating bond strength for the Ni-40TiO_2- and Ni-20TiO_2-20Al_2O_3-coated specimens was evaluated in accordance with the ASTM Standard C-633-2013 by the help of Bond Strength Testing Machine (Make: Instron, Tamil Nadu, India). Prior to the tests for both the coated specimens, the cross section of two cylindrical specimens (one is uncoated and another is as-sprayed) having diameter 25.4 mm was glued together with an adhesive (HTK-Ultra bond 100). Total five tests were conducted, and the average value was calculated. The specimens were dried at a temperature of 170 °C to ensure the strong bond between the specimens.

Further, the authors had evaluated the surface roughness values of the as-sprayed specimens. The average of three readings of surface roughness was taken, and the values are reported in Table 7. Microhardness of the substrate steel, the top coated surface layer and the microhardness of the coating along its cross section was measured by microhardness tester (Wilson 402MVD Vickers Microhardness Tester, S/N-V2D259, USA) with digital display. An indenting load of 100 N was applied on the diamond indenter for penetration on the surface with an indentation dwell time of 20 s. The average of three readings was taken as the microhardness value of the coating. This analysis was carried out at IIT Ropar, Punjab, India.

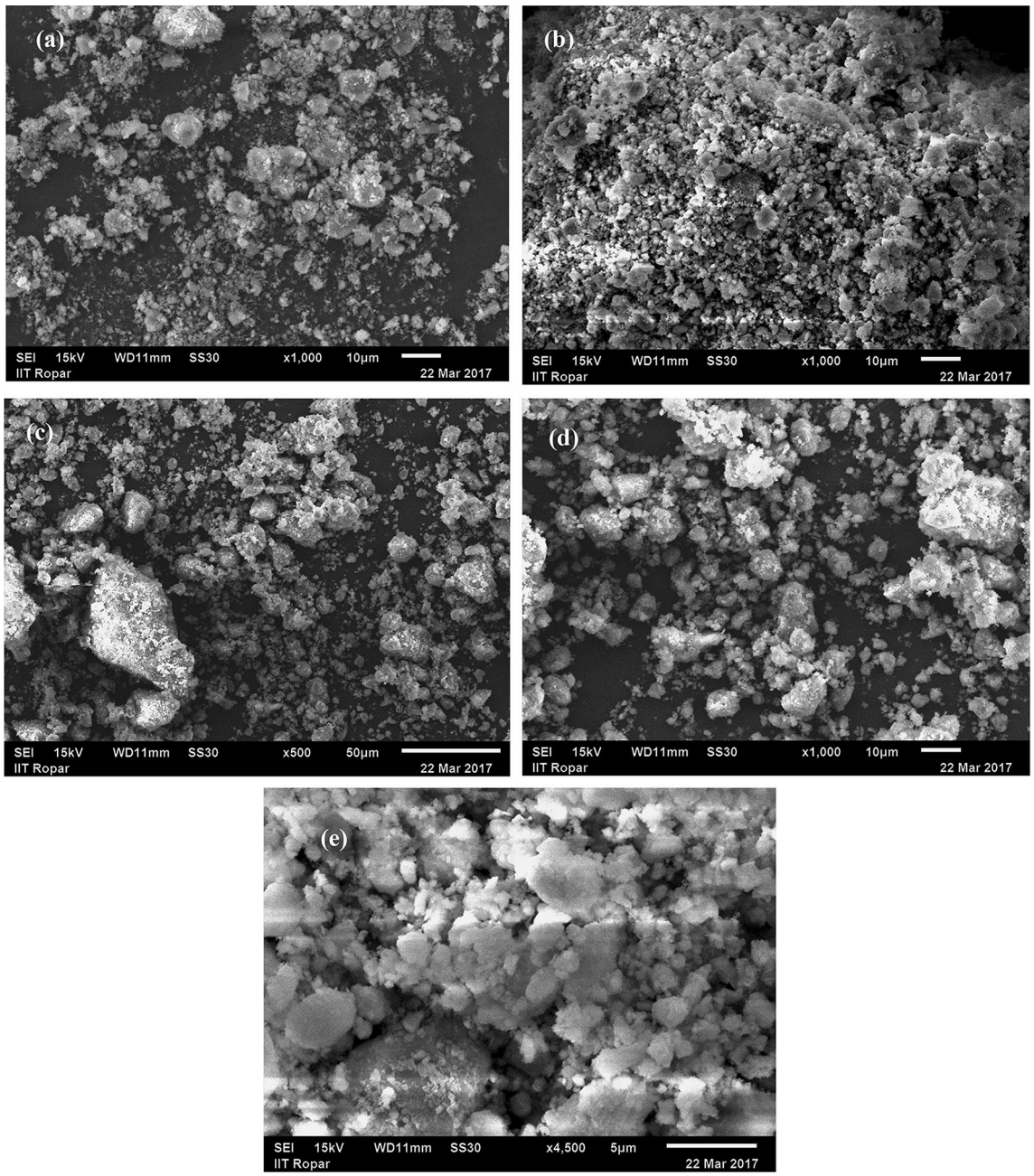

Fig. 8 SEM micrograph of synthesized Al_2O_3 powder ball-milled after (a) 12 h (b) 18 h (c) 24 h and (d) 30 h and (e) 40 h

Results and Discussion

Evaluation of Microstructure of Steel Substrate

The optical micrograph of ASTM-A743 standard CA6NM steel is shown in Fig. 1. The steel showed the presence of tempered martensite with some marks of retained austenite and delta ferrite. Similar micrographs of the steel were observed by Thibault et al. (Ref 20) and Espitia et al. (Ref 21).

Characterization of As-received Powders

Figure 2(a), (b) and (c) shows the SEM morphologies of pure nickel powder, micron-sized TiO_2 powder and micron-sized Al_2O_3 powder, respectively. The pure nickel

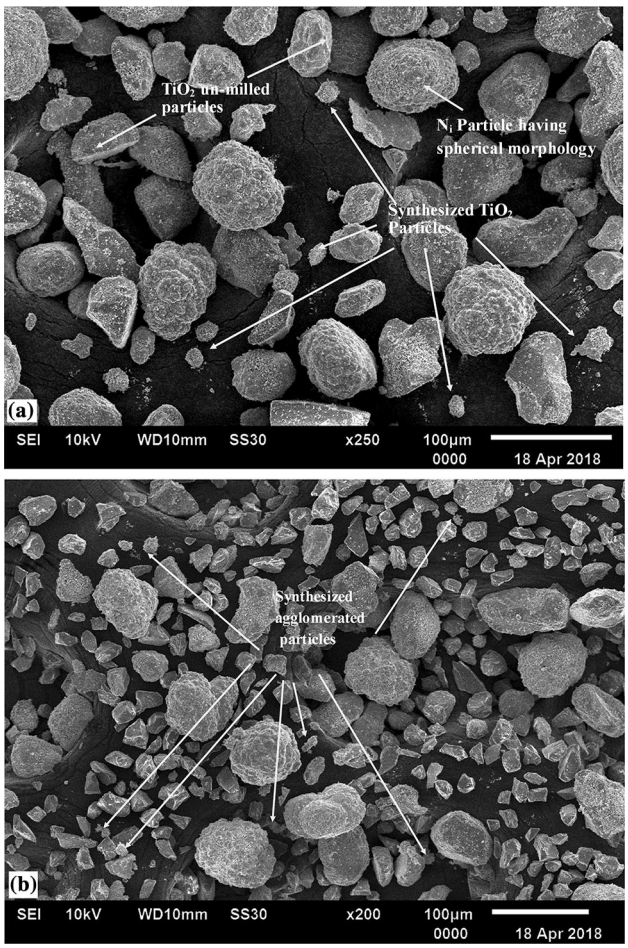

Fig. 9 SEM morphology of the HVFS powders: (a) Ni-40TiO_2 powder, (b) Ni-20TiO_2-20Al_2O_3 powder

powder particles were possessing spherical morphology (Fig. 2a). The TiO_2 and Al_2O_3 powder particles had sharp conical edges showing angular morphology (Fig. 2b and c). XRD graphs of Ni, TiO_2 and Al_2O_3 coating powders (as-received) are shown in Fig. 3 and 4 on reduced scales. Nickel was identified as the main intensity phase in the XRD analysis of pure nickel powder (Fig. 3). In the case of micron-sized TiO_2 powder (Fig. 4a), titanium oxide was identified as a very strong phase. In the unmilled TiO_2 powder, the presence of the tetragonal structure of anatase compound was revealed. Figure 4(b) depicts the XRD diffractogram of Al_2O_3 powder which showed the presence of alumina phase.

DLS Analysis of Synthesized Nanostructured TiO_2 Powder and Al_2O_3 Powder

Micron-sized (< 100 µm) TiO_2 powder and Al_2O_3 powder were ball-milled in the high-speed ball milling machine under a vacuum environment for the duration up to 30 h and 40 h, respectively. Thereafter, the prepared powders were analyzed at different intervals by dynamic light scattering (DLS) analysis. For titania powder, the specimens were analyzed after 6, 12, 18, 24 and 30 h, and for alumina powder, the specimens were analyzed after 6, 15, 18, 30 and 40 h. The average particle size (d50) distribution (PSD) analysis of the ball-milled TiO_2 powder at 18 h and Al_2O_3 powder at 30 h is shown in Fig. 5(a) and (b), respectively. Figure 5(a) reveals the size distribution of TiO_2 nanostructured particles. It was observed in the range from 60 to 1000 nm. Pass percentage and passing channels were the two parameters used by the test rig in the analysis of nanostructured particle. The average particle size was recorded on the Delsa Nano instrument as 185 nm. Some minor peaks in the range of less than 10 nm were also observed. The observed particle size range from 60 to 1000 nm might be due to the possibility of agglomerated particles. Furthermore, the polydispersity index (PDI) was evaluated as 0.29 after the test. The particle size distribution of the nanostructured Al_2O_3 particles was found to be in the range of 100-1000 nm (Fig. 5b). The average particle size value was measured as 216 nm. Figure 6(a) and (b) shows the plot of particle size of the powders versus the milling time in hours for TiO_2 and Al_2O_3 powders, respectively. The 18-h-milled TiO_2 powder and 30-h-milled Al_2O_3 powder were found to have the lowest particle sizes among all and thus further considered for mechanical blending in the Ni matrix to obtain the desired coating composition.

SEM Analysis of Synthesized Nanostructured TiO_2, Al_2O_3 and Prepared Coating Powders

Further, Fig. 7 and 8 shows the SEM morphology of the titania powder specimens milled after 12, 18, 24 and 30 h and of alumina powder specimens milled after 12, 15, 18, 30 and 40 h, respectively. The nanostructured TiO_2 powders (Fig. 7) appeared as clusters of agglomerated irregular (non-spherical) particles. The mechanism involved in mechanical milling was continuously fracturing and welding (recombination of smaller particles into agglomerates). This cycle continued with the milling process. After 12 h of milling, the average particles appeared flattened due to compressive forces under the collision impact of milling balls. Powder particles appeared soft at the edges. Subsequently, after 18 h milling time, the particles appeared agglomerated with the presence of small sharp edges. After 24 h of milling time, the particles showed the morphology of agglomerates. On further milling to 30 h, considerable refinement of particle/agglomerate size seemed to take place due to fracturing.

The SEM morphology of synthesized nanostructured Al_2O_3 powder particles after 12 h of milling time is shown

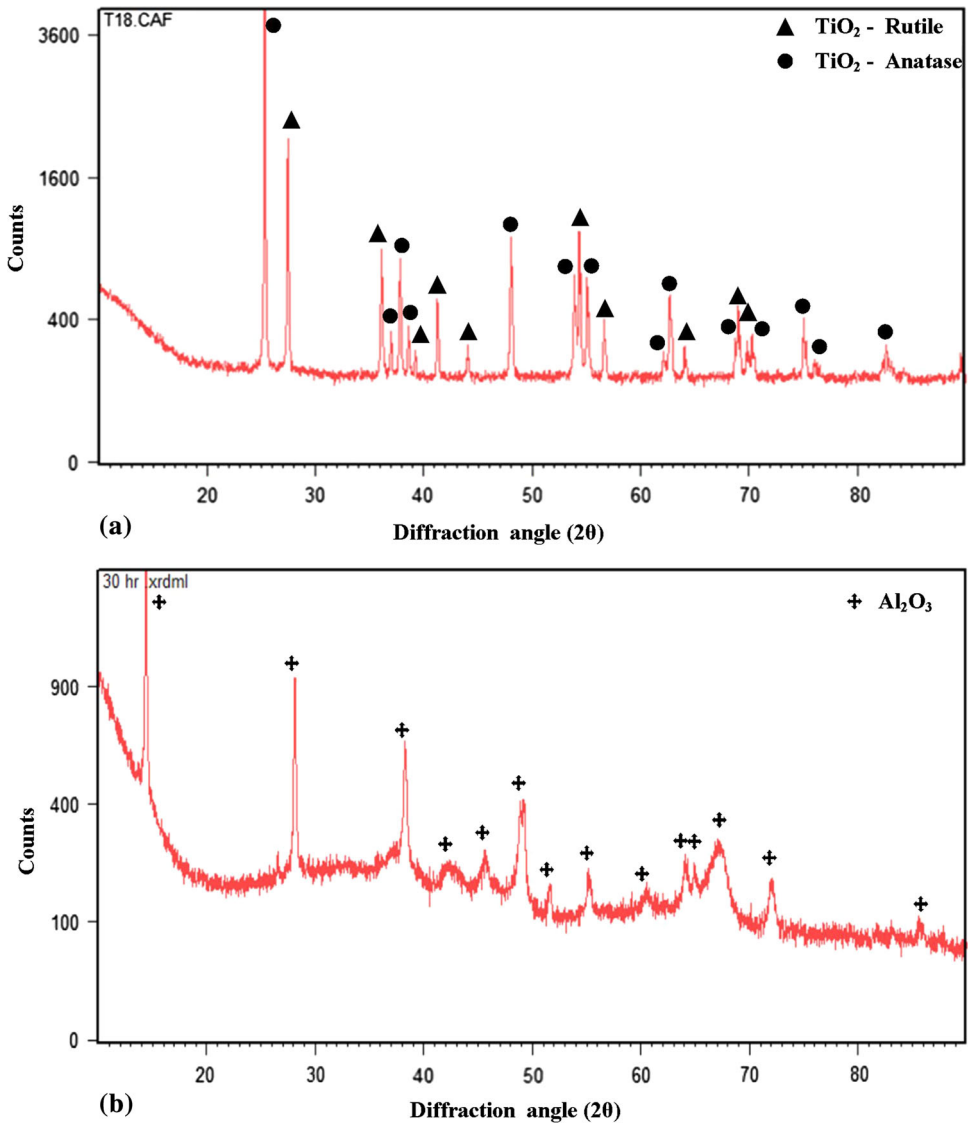

Fig. 10 X-ray diffraction pattern of (a) synthesized TiO_2 powder and (b) synthesized Al_2O_3 powder

in Fig. 8(a). Irregular small and large-sized particles were observed. After milling, some of the aggregates were observed with sharp edges and some were having spherical morphology. After 15 h of milling time, as shown in Fig. 8(b), alumina particles appeared flattened with reduced size. The flattened particles were fractured under the continuous action of crushing forces applied by the milling balls in the jar. The particles were seen uniformly distributed. As the milling progressed beyond 18 h of milling time, the agglomerated particles formed the cluster of particles (Fig. 8c). Some smaller-sized particles stick onto the surface of bigger particles. After 30 h of milling time, the particles were observed to be fractured again (Fig. 8d). Few particles appeared in the form of clusters and many were possessing fractured flat shape morphology. After 40 h of milling time, the particles appeared in the form of fractured particles with the majority of them agglomerated together (Fig. 8e). Figure 9(a) and (b) shows the SEM micrographs of Ni-40TiO_2 and Ni-20TiO_2-20Al_2O_3 composite powders, respectively. The composite powders consisted of both micron- and nanostructured sized particles. The two composite powders were found to have a mixer of three descriptions of particles which constitute spherical, angular and lumps of particles dispersed into it. In the SEM micrograph of Ni-40TiO_2 composite powder, nanostructured nickel powders were found to have spherical morphology and the titania particles of angular shape were found in variable sizes (Fig. 9a). In the case of

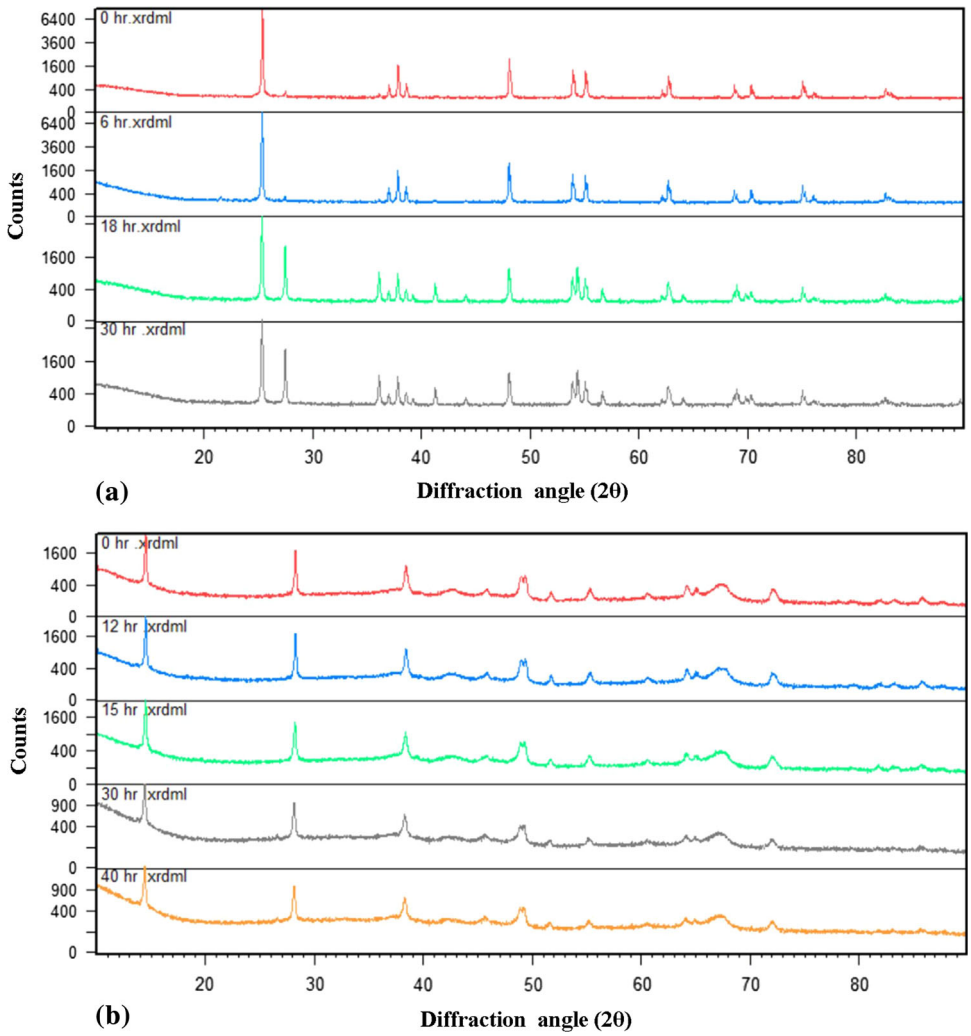

Fig. 11 X-ray diffraction patterns for ball-milled (a) TiO_2 powder and (b) Al_2O_3 powder at different hours

Ni-20TiO_2-20Al_2O_3 composite powder, micron-sized alumina and titania were seen well blended together in the nickel matrix along with the nanostructured particles attached to them (Fig. 9b).

XRD Analysis of Synthesized Nanostructured TiO_2, Al_2O_3 and Prepared Coating Powders

In the synthesized titania powder after 18 h of milling time, anatase and rutile phases were observed (Fig. 10a) in the XRD analysis, whereas in the case of synthesized alumina powder after 30 h of milling time, alumina was observed as the main phase shown in Fig. 10(b). Figure 11(a) and (b) shows the pattern of peaks for different milling times of TiO_2 and Al_2O_3, respectively.

The phase change in the milled titania powder was not observed during the initial period of the milling time. After a longer time, the anatase phase of the titania powder was changed to rutile phase. Similar results were obtained by Furlani et al. (Ref 22). The authors milled the titania powder for several hours in a planetary high-speed ball mill and observed the transformation of the anatase phase of titania into the rutile phase. Further, Chen et al. (Ref 23) and Ranade et al. (Ref 24) proposed different techniques for producing the nanostructured TiO_2 powder and reported that the longer milling time resulted in the generation of heat due to the shearing action of the balls. This increased the temperature of milling process. The increase in temperature during the process resulted in the change of the anatase phase of titania into the rutile phase. Additional,

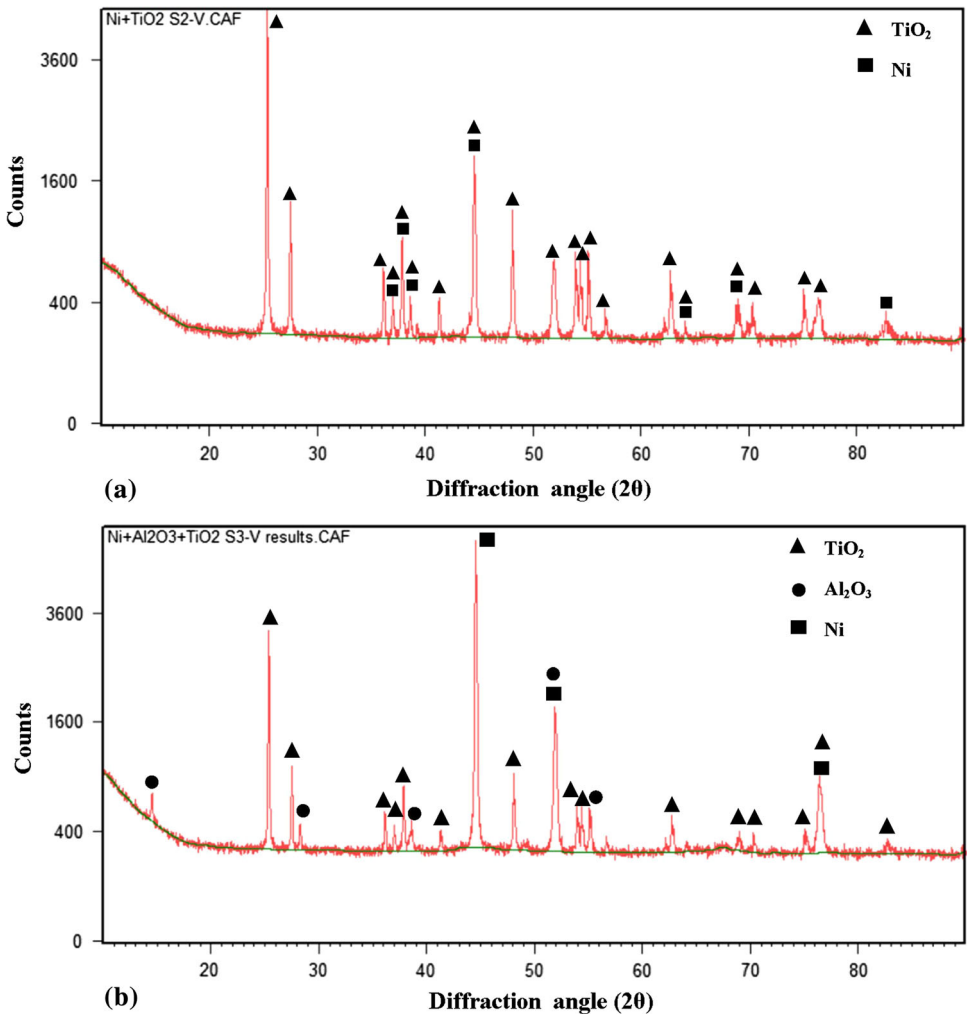

Fig. 12 X-ray diffraction pattern of (a) Ni-40TiO_2 powder and (b) Ni-20TiO_2-20Al_2O_3 coating feedstock powders

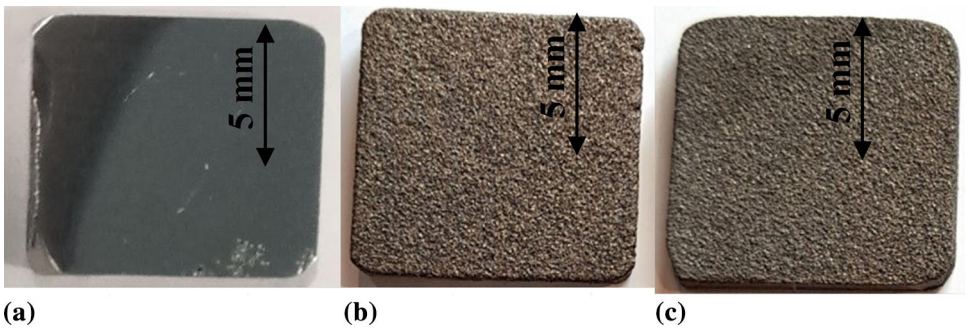

Fig. 13 Macrographs of (a) uncoated CA6NM hydro turbine steel specimen with HVFS, (b) Ni-40TiO_2 coating and (c) Ni-20TiO_2-20Al_2O_3 coating

higher-intensity and broader peaks were identified after 18 h milling time for TiO_2 powder and after 30 h of milling time for Al_2O_3 powder. Zak et al. (Ref 25) conducted the x-ray analysis of the ZnO nanoparticles by Williamson–Hall and the size strain plot method. The crystalline size of the powder was identified by measuring the broadening of the peaks at this position. By using this method, the authors revealed that broader peaks in the x-ray pattern indicated the lesser crystalline size of the nanoparticles, thus indicating the reduction in the crystalline size. In the present study, the average crystalline size of the TiO_2 and Al_2O_3 was found as 28 and 37 nm, respectively. Figure 12(a) and (b) shows the XRD diffractograms of the prepared Ni-40TiO_2 and Ni-20TiO_2-20Al_2O_3 composite coating powders. In the case of Ni-40TiO_2 powder, TiO_2 was observed as the strong-intensity

phase and Ni was identified as the medium-intensity phase. The XRD analysis of Ni-20TiO_2-20Al_2O_3 composite coating powder revealed the presence of Ni and TiO_2 as the strong-intensity phases. Al_2O_3 was identified as the medium-intensity phase (Fig. 12b).

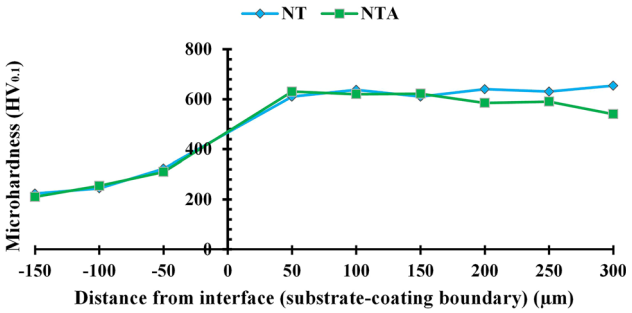

Fig. 14 Microhardness profile of HVFS Ni-40TiO_2 and Ni-20TiO_2-20Al_2O_3 coatings along the cross section

Characterization of As-Sprayed Specimens

Mechanical Characterization

Table 7 summarizes the mechanical properties obtained for the uncoated steel and the as-sprayed specimens. The coating porosity was found in the range of 0.8-2.0% for the Ni-40TiO_2 coating, whereas for the Ni-20TiO_2-20Al_2O_3 coating, the value ranges between 1.6 and 3.6%. The analysis of the porosity is very important for the study of erosion wear in hydropower applications. The dense coating usually exhibits good resistance to slurry erosion. The magnitude of porosity obtained in the Ni-20TiO_2-20Al_2O_3 coating was in close tolerance with the porosity obtained by various researchers. Kumar et al. (Ref 7) conducted a study on HVFS Ni-15TiO_2-5Al_2O_3-coated substrate and observed similar porosity values. The authors opined that the higher values of porosity observed in the Ni-15TiO_2-5Al_2O_3 coating might be due to the marginal higher

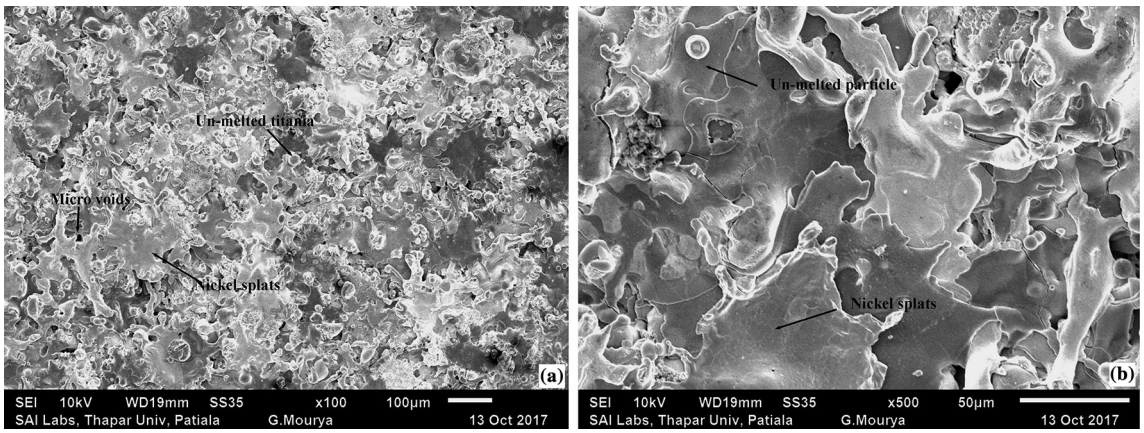

Fig. 15 Surface scale morphology of the as-sprayed Ni-40TiO_2 coating at (a) 100X magnification and (b) 500X magnification

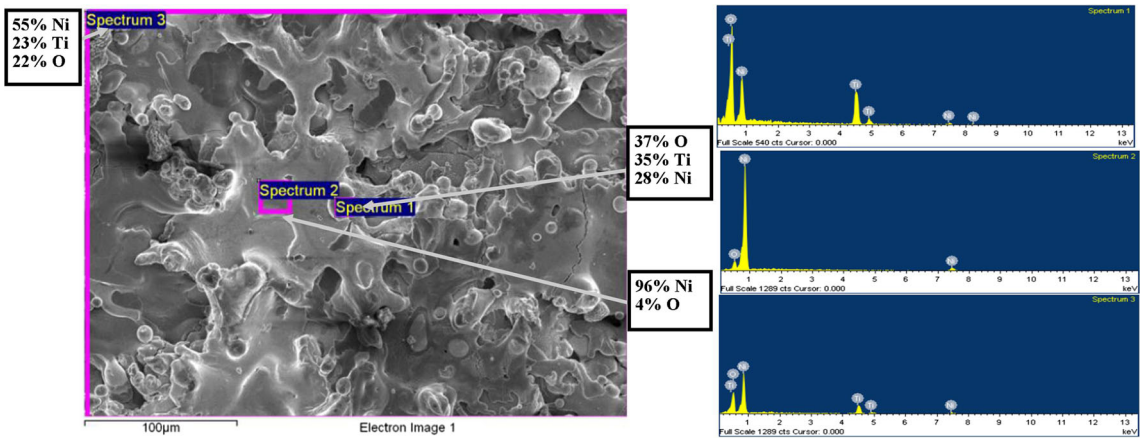

Fig. 16 Surface scale morphology and EDS analysis of CA6NM hydro turbine steel with HVFS Ni-40TiO_2 coating showing elemental composition (%) at selected

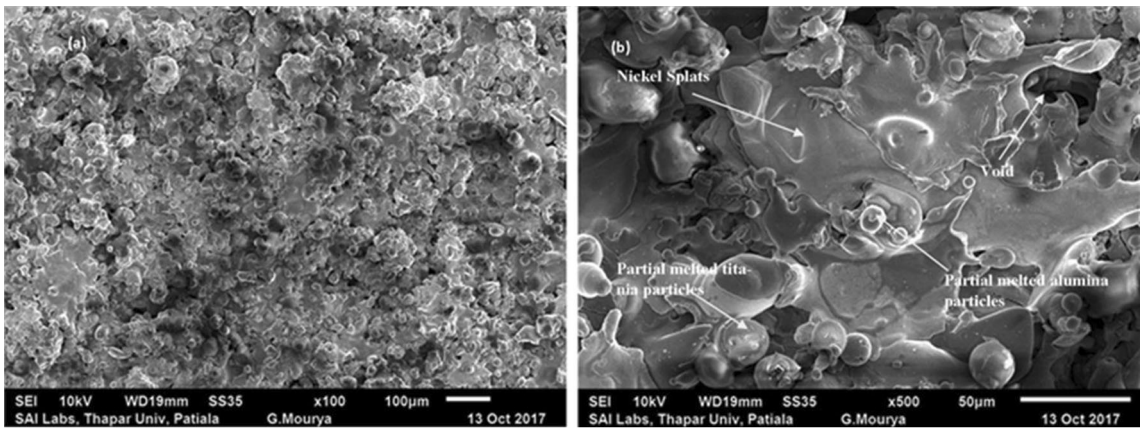

Fig. 17 Surface scale morphology of the as-sprayed Ni-20TiO_2-20Al_2O_3 coating at (a) 100X magnification and (b) 500X magnification

melting point of Al_2O_3 in comparison with Ni and TiO_2. The alumina was left in an unmelted/semi-melted state embedded into the nickel and TiO_2 splats. The voids formed due to this might created high exposure of the metal surface to the slurry particles during the hydro-application reported by the author while studying the behavior of the coating against slurry erosion. Further, Tomaszek et al. (Ref 26) deposited the alumina composite with 40% TiO_2 coating by plasma spraying technique and also reported the higher values of porosity up to 6%. On the other hand, a lower value of porosity was observed in the Ni-40TiO_2 coating. Baghery et al. (Ref 27) and Hao et al. (Ref 28) reported in their study that TiO_2 nanoparticles dispersed in the Ni matrix filled the voids in the coating. This increased the surface area which further decreases the porosity in the coating.

Figure 13 shows the as-sprayed micrographs of the coated specimens. Both the Ni-40TiO_2 and Ni-20TiO_2-20Al_2O_3 coatings possessed dark and light gray colors, respectively. Moreover, the Ni-40TiO_2 coating appeared lustrous also. The coated surface was smooth and was free from any visible surface cracks. The average surface roughness values of the as-sprayed coating were limited to 6.61 ± 0.4 and 9.39 ± 0.4 µm for the Ni-40TiO_2 and the Ni-20TiO_2-20Al_2O_3 coatings, respectively. For predicting the coating performance, estimation of the bond strength is very much important in the study. In the current investigation, ASTM standard C-633 was used for evaluating the degree of adhesion of the coating with the substrate (Ref 29). According to the Lima et al. (Ref 30) and Sundararajan et al. (Ref 31), the number of spraying passes, surface roughness at the coating/metal interference and surface roughness after coating are the main parameters responsible for better adhesion strength. The bond strength evaluated for the Ni-40TiO_2 and Ni-20TiO_2-20Al_2O_3 coatings was 66.4 and 61.7 MPa, respectively. The adhesion failure was observed in the Ni-40TiO_2-coated specimens, whereas glue failure was observed in the case of Ni-20TiO_2-20Al_2O_3-coated specimens. Kumar et al. (Ref 9) deposited the micron-sized compositions of Ni-20TiO_2 and Ni-15TiO_2-5Al_2O_3 coatings on the CA6NM steel by HVFS process. The bond strength values for both the coatings were obtained as 55.61 and 57.12 MPa, respectively. It is interesting to notice that the bond strength values obtained in the present study were higher than those obtained by other researchers. The observations state that the addition of 40% TiO_2 in micron size and nanostructured size might be useful. The values of fracture toughness were recorded as 1.8 ± 0.10 and 1.6 ± 0.20 MPa-$m^{1/2}$ for the Ni-40TiO_2 and the Ni-20TiO_2-20Al_2O_3 coatings, respectively. The density (obtained by Eq 2) of the Ni-40TiO_2 and Ni-20TiO_2-20Al_2O_3coatings was evaluated as 6100 and 5910 kg/m^3.

Estimation of Microhardness

The microhardness values are plotted with respect to distance from the substrate/coating interface as shown in Fig. 14. The microhardness values for the Ni-40TiO_2 coating and Ni-20TiO_2-20Al_2O_3 coating lie in the range of

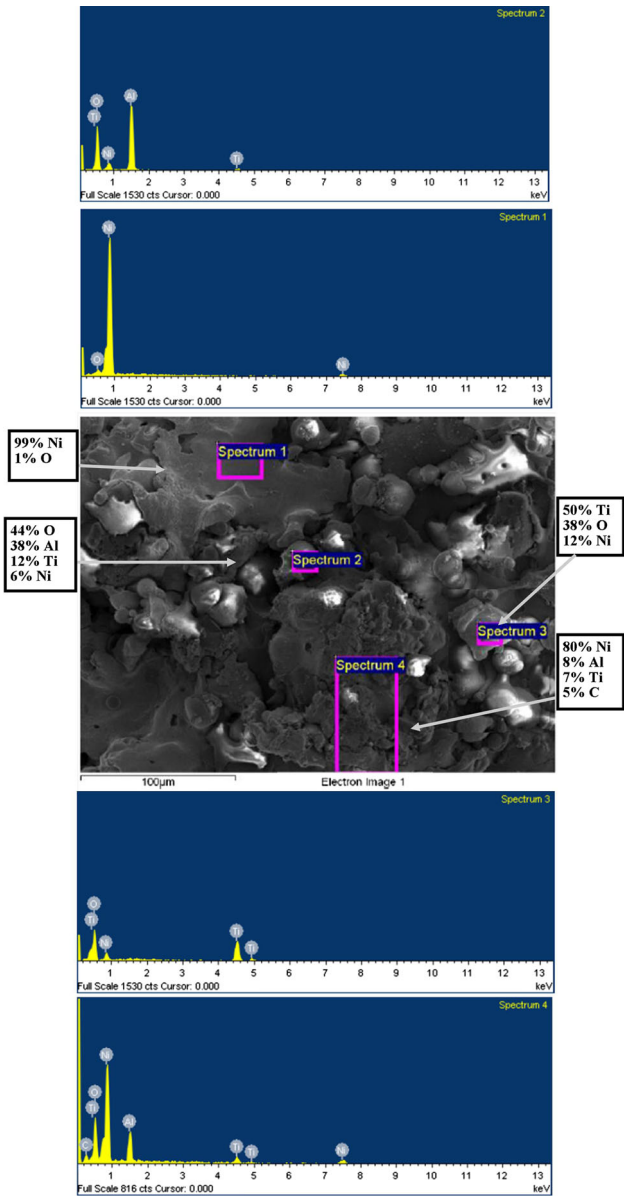

Fig. 18 Surface scale morphology and EDS analysis of CA6NM hydro turbine steel with HVFS Ni-20TiO_2-20Al_2O_3 coating showing elemental composition (%) at selected points

560 to 650 and 464 to 698 $HV_{0.1}$, respectively, with an average value of 605 ± 37 and 585 ± 33 $HV_{0.1}$ for the two coatings, respectively. The substrate steel has an average microhardness of 247 ± 18 $HV_{0.1}$. Grewal et al. (Ref 6) prepared the composite of Ni-$Al_2O_3$and deposited this composition on the CA6NM hydro turbine steel by the HVFS process. The authors observed that the presence of the γ phase of alumina imparted the higher hardness values in the deposited coating. In the present experimental work, the Ni-40TiO_2 coating showed more hardness in comparison with the Ni-20TiO_2-20Al_2O_3coating. This might be due to the lower porosity values attained by the Ni-40TiO_2 coating. Further, the presence of brittle unmelted alumina particles might have created the small vacant pores in the Ni-20TiO_2-20Al_2O_3 coating. While deposition of the coating, the nanostructured sized alumina particles might get agglomerated during the melting process and the proper binding with the matrix phase was not achieved. This led to creation of voids on the surface and cross section of the coating (porous structure). Grewal et al. (Ref 6) and Sundararajan et al. (Ref 31) found a similar observation in their research studies. The value of hardness was varied along a distance from the interface of coating substrate. In the present study, the authors revealed that the addition of TiO_2 in the Ni-rich matrix increased the microhardness of the coating. Baghery et al. (Ref 27) deposited the Ni-TiO_2 nanostructured composite coating on a low-carbon steel substrate. The authors observed the similar characteristics of the coating.

SEM and EDS Analyses of As-Sprayed Coating

Figure 15 shows the SEM micrograph of the HVFS Ni-40TiO_2 coating deposited on the turbine steel. The micrograph of the coated region appeared stratum in nature. The EDS analysis of the as-sprayed coating at spectrum 1 to spectrum 3 on the surface is presented in Fig. 16 which indicates the presence of Ni, Ti and O on the coated surface. The surface micrograph and EDS analysis of Ni-20TiO_2-20Al_2O_3-sprayed coating are shown in Fig. 17 and 18, respectively. It was observed that all the elements of the coating are uniformly dispersed over the surface. Unmelted particles of titania and alumina were observed. Partially melted alumina appeared in white shiny color, whereas partially melted titania appeared in dull grayish color. The EDS examination of the as-sprayed coating indicates the existence of Ni, Al, Ti at spectrum 1 to spectrum 4 along with the presence of O.

XRD Analysis

The x-ray diffraction patterns for the HVFS, Ni-40TiO_2- and Ni-20TiO_2-20Al_2O_3-coated CA6NM steels are shown in Fig. 19 and 20, respectively. For the Ni-40TiO_2 coating, Ni was observed as the strong-intensity intermetallic phase. TiO_2 phase was identified as the medium-intensity phase. In the case of Ni-20TiO_2-20Al_2O_3 coating, nickel was observed as the strong-intensity phase. TiO_2 and Al_2O_3 were observed as medium-intensity phases in the as-

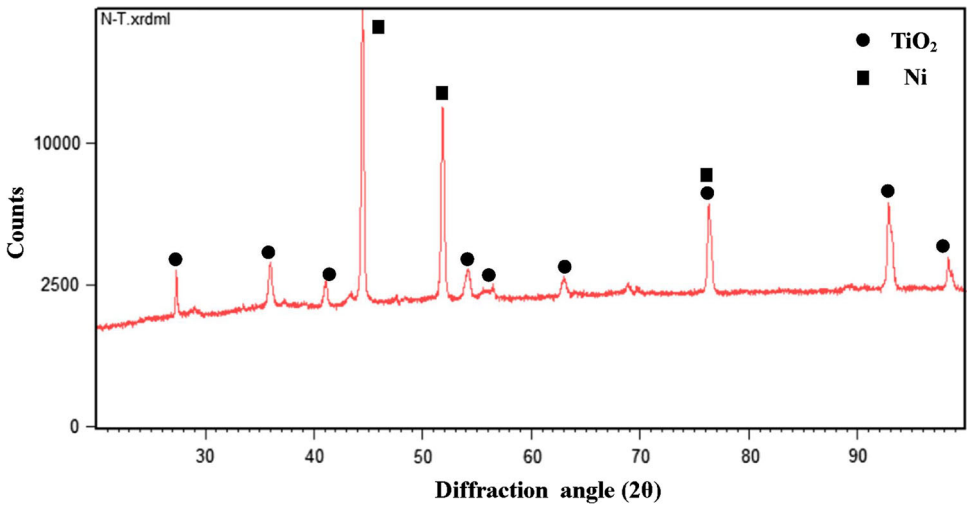

Fig. 19 X-ray diffraction pattern for the HVFS Ni-40TiO_2-coated CA6NM hydro turbine steel

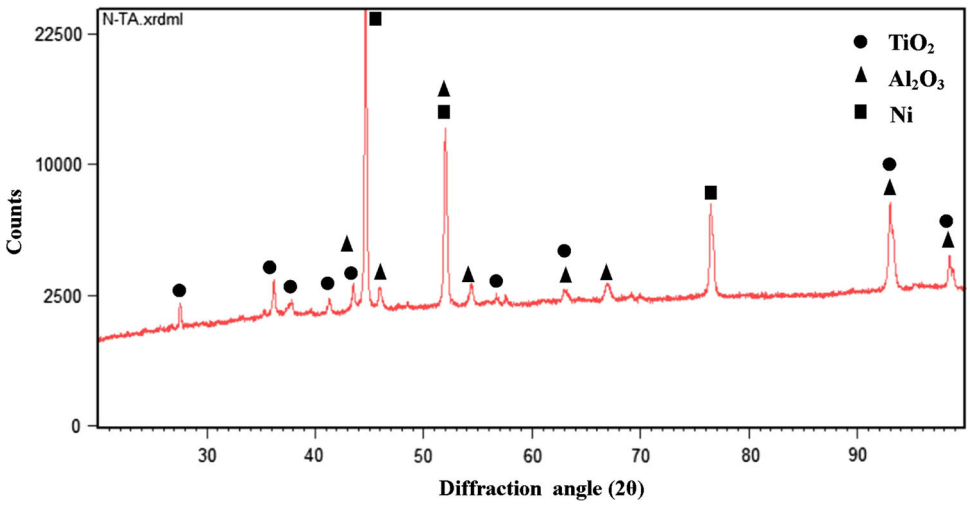

Fig. 20 X-ray diffraction pattern for the HVFS Ni-20TiO_2-20Al_2O_3-coated CA6NM hydro turbine steel

sprayed coating. Similar results were reported by Kumar et al. (Ref 9).

Microstructural Characterization and Compositional Analysis of As-Sprayed Coating (Cross Section)

Cross-sectional SEM morphologies of the as-sprayed Ni-40TiO_2 and Ni-20TiO_2-20Al_2O_3 coatings are shown in Fig. 21(a) and (b), respectively. Both the coatings were found to have similar morphologies with the presence of laminar splats. The splats were found to be intact with each other. The coatings were found to be dense and intact with nearly uniform thickness. The coatings were in good adherence with the substrate steel. The interface was free from defects. Marginal presence of superficial voids was observed in the Ni-20TiO_2-20Al_2O_3 coating as shown in Fig. 22(b). The EDS analysis of both the coated specimens indicates that the dark phase in the microstructure contained the Ti, Al and O, thereby indicating the TiO_2 and Al_2O_3 phases. The lighter region in the micrographs depicts the Ni matrix. The average thickness of the Ni-40TiO_2 and Ni-20TiO_2-20Al_2O_3 coatings was measured as 422 ± 10 and 354 ± 10 μm, respectively.

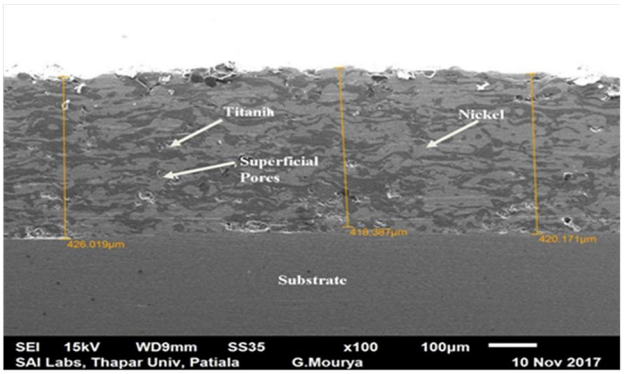

(a)

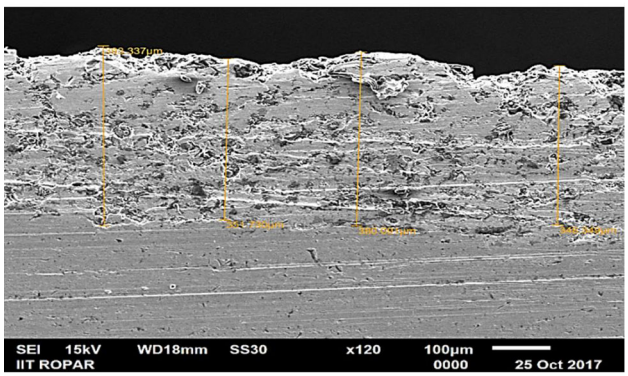

(b)

Fig. 21 SEM micrographs showing cross-sectional morphology of HVFS (a) Ni-40TiO_2 coating and (b) Ni-20TiO_2-20Al_2O_3 coating on CA6NM hydro turbine steel specimen

Composition image (SE) and x-ray mappings of the as-sprayed HVFS coatings show distinct layers of the coating and substrate (Fig. 23 and 24). The elemental mappings for both the coatings showed the basic elements of the powders that are Ni, Ti, Al and O dispersed in the coated region. It is clear from Fig. 23 that the nickel exists throughout the thickness of the coating and at the places where it is absent, titanium and oxygen were found. Some amount of carbon was also found throughout the coating composition. Figure 24 shows the presence of nickel, oxygen and carbon throughout the coating. Aluminum and titanium were observed in the coating in the form of clusters along with the oxygen. Iron was restricted to the base steel only. Similar cross-sectional microstructures were observed by other researchers also (Ref 9).

Conclusion

1. The Ni-40TiO_2 and Ni-20TiO_2-20Al_2O_3 composite coatings were well developed on the chosen CA6NM hydro turbine steel by the HVFS process. The values of porosity for the HVFS nanostructured composite coatings was recorded in the range of 0.8 to 3.6%. The Ni-40TiO_2 coating showed lesser porosity than the Ni-20TiO_2-20Al_2O_3 coating.
2. The TiO_2- and Al_2O_3-blended compositions were found to have a composite-like microstructure where TiO_2- and Al_2O_3-rich splats were seen uniformly dispersed in the Ni matrix with the presence of melted, semi-melted and unmelted particles. The cross-sectional micrographs showed that the interface between the substrate and the coatings was free of discontinuities.
3. The microhardness was found to vary with the distance along the cross section of the coatings. So far as the upper values of the hardness range are concerned, Ni-40TiO_2 coating on CA6NM steel showed an upper limit of 605 ± 37 HV, while Ni-20TiO_2-20Al_2O_3 coating exhibited an upper limit of 585 ± 33 HV.
4. The higher bond strength value and the fracture toughness value were obtained in the Ni-40TiO_2 coating. The measured value was 66.4 MPa and 1.8 ± 0.2 MPa-$m^{1/2}$, respectively.

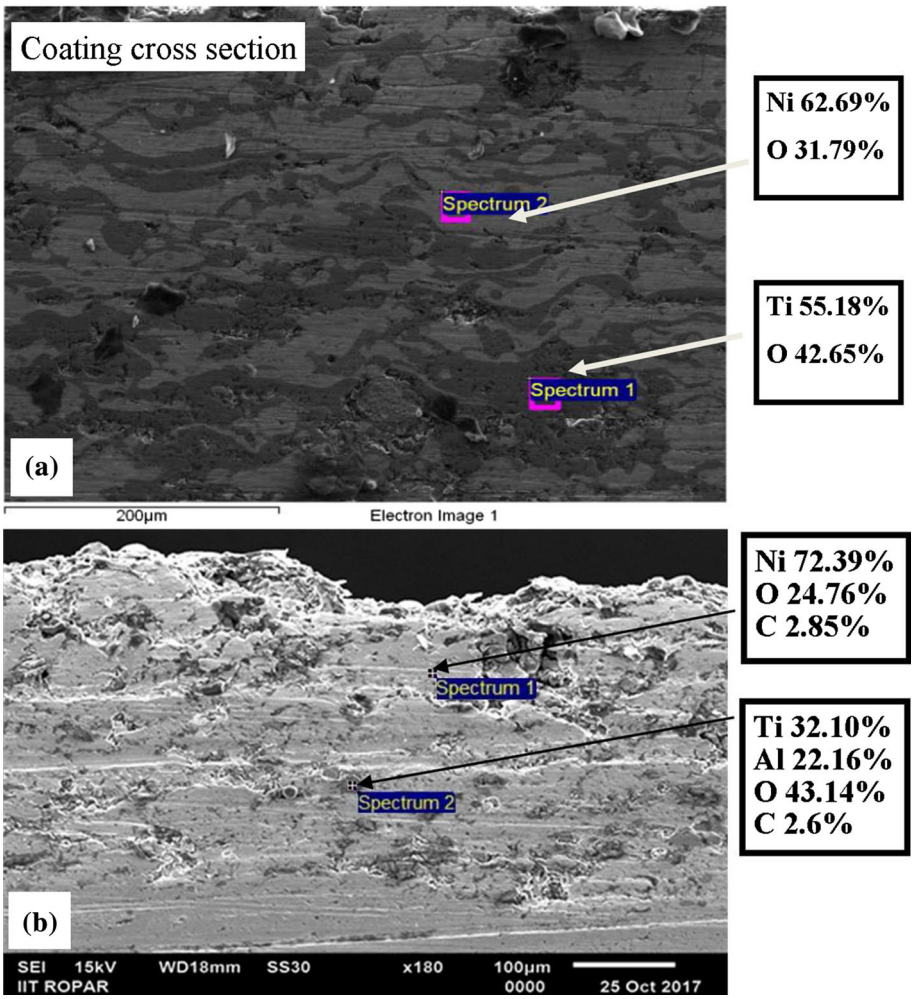

Fig. 22 Morphology and variation of elemental composition across the cross section of HVFS (a) Ni-40TiO_2 coating and (b) Ni-20TiO_2-20Al_2O_3 coating on CA6NM steel specimen

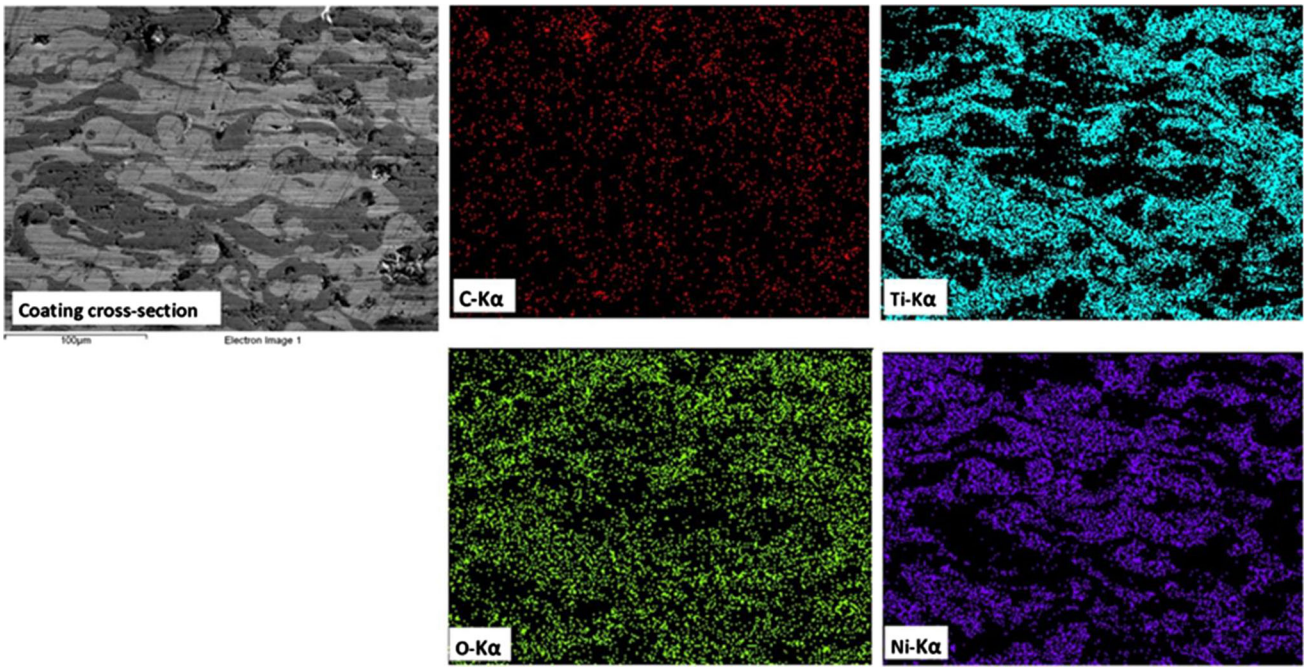

Fig. 23 X-ray mappings of the cross section of HVFS Ni-40TiO_2-coated CA6NM hydro turbine steel

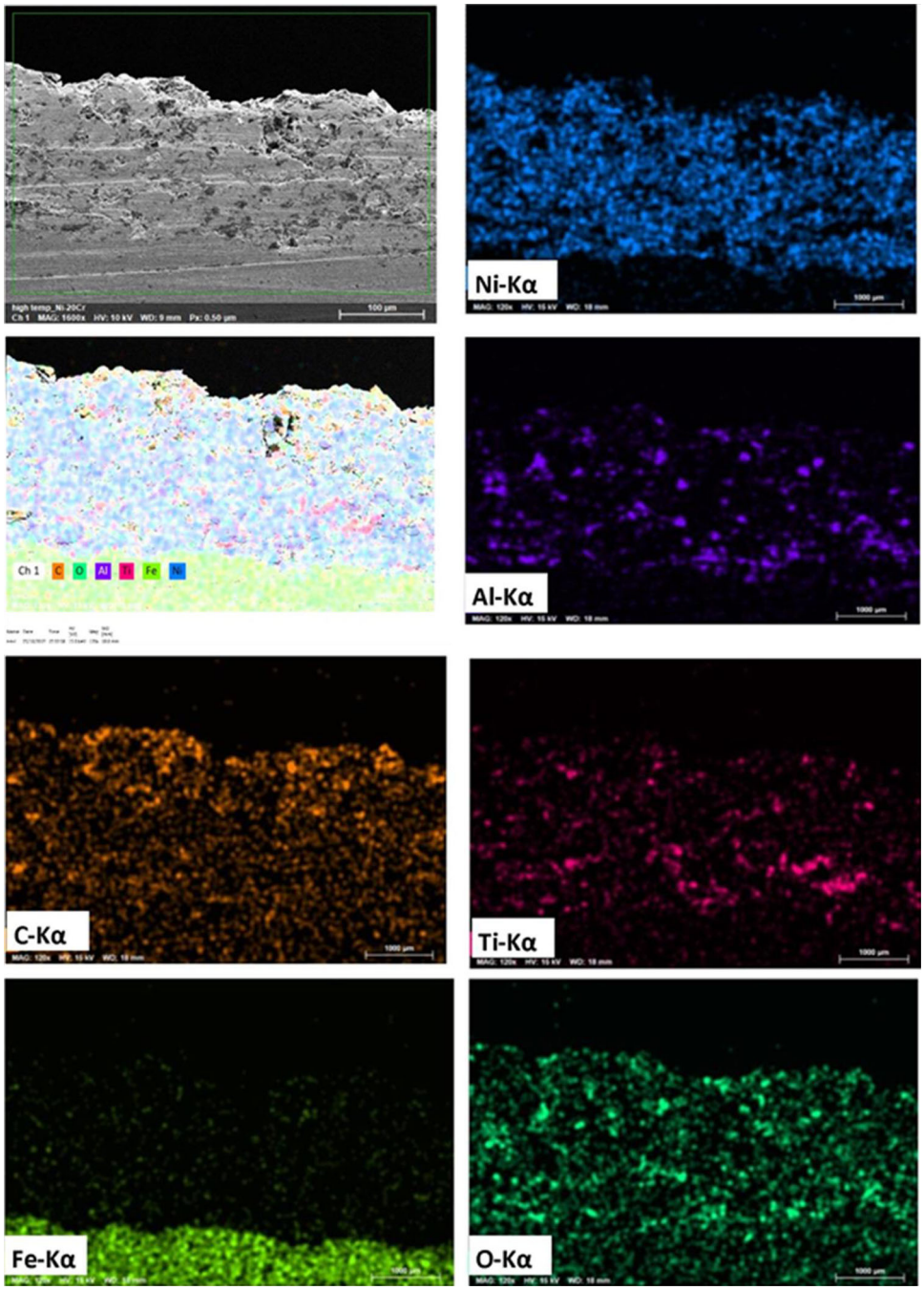

Fig. 24 X-ray mappings of the cross section of HVFS Ni-20TiO_2-20Al_2O_3-coated CA6NM hydro turbine steel

Acknowledgment The authors thankfully acknowledge all the essential research facilities required for the completion of this project provided by Indian Institute of Technology Ropar, India, and Indian Institute of Technology, Roorkee. The authors would like to express sincere thanks to IKG, Punjab Technical University, Punjab, India, for supporting this research work.

References

1. V. Sharma, M. Kaur, and S. Bhandari, Slurry Jet Erosion Performance of High-Velocity Flame-Sprayed Nano Mixed Ni-40Al_2O_3 Coating in Aggressive Environment, *Proc. Inst. Mech. Eng. Part J J. Eng. Tribol.*, 2019, https://doi.org/10.1177/1350650118822426
2. M.K. Padhy and R.P. Saini, Effect of Size and Concentration of Silt Particles on Erosion of Pelton Turbine Buckets, *Energy*, 2009, **34**(10), p 1477-1483. https://doi.org/10.1016/j.energy.2009.06.015
3. M.K. Padhy and R.P. Saini, A Review on Silt Erosion in Hydro Turbines, *Renew. Sustain. Energy Rev.*, 2008, **12**(7), p 1974-1987
4. V. Sharma, M. Kaur, and S. Bhandari, Slurry Erosion Performance Study of High Velocity Flame Sprayed Ni-Al_2O_3 Coating Under Hydro Accelerated Conditions, *Mater. Res. Express*, 2019, **2019**(6), p 1-17. https://doi.org/10.1088/2053-1591/ab1927
5. H.S. Grewal, A. Agrawal, H. Singh, and B.A. Shollock, Slurry Erosion Performance of Ni-Al_2O_3 based Thermal-Sprayed Coatings: Effect of Angle of Impingement, *J. Therm. Spray Technol.*, 2014, **23**(3), p 389-401
6. H.S. Grewal, H. Singh, and A. Agrawal, Microstructural and Mechanical Characterization of Thermal Sprayed Nickel-Alumina Composite Coatings, *Surf. Coat. Technol.*, 2013, **216**, p 78-92. https://doi.org/10.1016/j.surfcoat.2012.11.029
7. R. Kumar, S. Bhandari, and A. Goyal, Slurry Erosion Performance of High-Velocity Flame-Sprayed Ni-20Al_2O_3 and Ni-10Al_2O_3-10TiO_2 Coatings Under Accelerated Conditions, *J. Therm. Spray Technol.*, 2017, **26**(6), p 1279-1291
8. B.E. Naveena, R. Keshavamurthy, and N. Sekhar, Slurry Erosive Wear Behaviour of Plasma-Sprayed Flyash–Al_2O_3 Coatings, *Surf. Eng.*, 2017, **33**(12), p 925-935
9. R. Kumar, S. Bhandari, and A. Goyal, Synergistic Effect of Al_2O_3/TiO_2 Reinforcements on Slurry Erosion Performance of Nickel-Based Composite Coatings, *Proc. Inst. Mech. Eng. Part J J. Eng. Tribol.*, 2017, https://doi.org/10.1177/1350650117736487
10. D. Wang, Z. Tian, S. Wang, L. Shen, and Y. Huang, Solid Particle Erosion Behaviour of Plasma-Sprayed Conventional and Nanostructured Al_2O_3-13 wt% TiO_2 Ceramic Coatings, *Trans. Indian Ceram. Soc.*, 2015, **74**(2), p 90-96. https://doi.org/10.1080/0371750X.2015.1036169
11. M. Benegra, M. Magnani, H. Goldenstein, O. Maranho, and G. Pintaude, Abrasion and Corrosion Resistance of New Ni-Based Coating Deposited by HVOF Thermal Spray Process, *Surf. Eng.*, 2010, **26**(6), p 463-468. https://doi.org/10.1179/026708410X12550773058144
12. B. Thiyagarajan and V. Senthilkumar, Experimental Studies on Fly-Ash Erosion Behavior of Ni-Cr Based Nanostructured Thermal Spray Coating in Boiler Tubes, *Mater. Manuf. Process.*, 2017, **32**(11), p 1209-1217. https://doi.org/10.1080/10426914.2016.1257798
13. C. Suryanarayana, Mechanical Alloying and Milling, *Prog. Mater. Sci.*, 2001, **46**(1–2), p 1-184. https://doi.org/10.1016/s0079-6425(99)00010-9
14. W. Chen, Y. He, and W. Gao, Electrodeposition of Sol-Enhanced Nanostructured Ni-TiO_2 Composite Coatings, *Surf. Coat. Tech.*, 2010, **204**(15), p 2487-2492. https://doi.org/10.1016/j.surfcoat.2010.01.036
15. S. Lajevardi and T. Shahrabi, Effects of Pulse Electrodeposition Parameters on the Properties of Ni-TiO_2 Nanocomposite Coatings, *Appl. Surf. Sci.*, 2010, **256**(22), p 6775-6781. https://doi.org/10.1016/j.apsusc.2010.04.088
16. G. Parida, D. Chaira, M. Chopkar, and A. Basu, Synthesis and Characterization of Ni-TiO_2 composite Coatings by Electro-Co-Deposition, *Surf. Coat. Technol.*, 2011, **205**(21–22), p 4871-4879. https://doi.org/10.1016/j.surfcoat.2011.04.102
17. M.L. Benea and L.P. Benea, Characterization of the WC Coatings Deposited by Plasma Spraying, *IOP Conf. Ser. Mater. Sci. Eng.*, 2015, **85**(1), p 012004
18. G.E. Kim, J. Falzon, J. Walker, F. Michael, and P. Nikki, Use of Nano-Particle Titanium Dioxide (n-TiO_2) Thermal Spray Coatings for Abrasion Resistance in Severe Service Applications, in *International Titanium Association*, 2010.
19. Y. Yang, D. Yan, Y. Dong, X. Chen, L. Wang, Z. Chu, J. Zhang, and J. He, Preparing of Nanostructured Al_2O_3-TiO_2-ZrO_2 composite Powders and Plasma Spraying Nanostructured Composite Coating, *Vacuum*, 2013, **96**, p 39-45. https://doi.org/10.1016/j.vacuum.2013.03.010
20. D. Thibault, P. Bocher, M. Thomas, J. Lanteigne, P. Hovington, and P. Robichaud, Reformed Austenite Transformation during Fatigue Crack Propagation of 13%Cr-4%Ni Stainless Steel, *Mater. Sci. Eng. A*, 2011, **528**(21), p 6519-6526. https://doi.org/10.1016/j.msea.2011.04.089
21. L.A. Espitia, L. Varela, C.E. Pinedo, and A.P. Tschiptschin, Cavitation Erosion Resistance of Low Temperature Plasma Nitrided Martensitic Stainless Steel, *Wear*, 2013, **301**(1–2), p 449-456. https://doi.org/10.1016/j.wear.2012.12.029
22. E. Furlani, E. Aneggi, C. de Leitenburg, and S. Maschio, High Energy Ball Milling of Titania and Titania-Ceria Powder Mixtures, *Powder Technol.*, 2014, **254**, p 591-596. https://doi.org/10.1016/j.powtec.2014.01.075
23. X. Chen and S.S. Mao, Titanium Dioxide Nanomaterials: Synthesis, Properties, Modifications and Applications, *Chem. Rev.*, 2007, **107**(7), p 2891-2959
24. M.R. Ranade, A. Navrotsky, H.Z. Zhang, J.F. Banfield, S.H. Elder, A. Zaban, P.H. Borse, S.K. Kulkarni, G.S. Doran, and H.J. Whitfield, Energetics of Nanocrystalline TiO_2, *Proc. Natl. Acad. Sci. USA*, 2002, **99**(2), p 6476-6481. https://doi.org/10.1073/pnas.251534898
25. A.K. Zak, W.H.A. Majid, M.E. Abrishami, and R. Yousefi, X-Ray Analysis of ZnO Nanoparticles by Williamson-Hall and Size-Strain Plot Methods, *Solid State Sci.*, 2011, **13**(1), p 251-256
26. R. Tomaszek, L. Pawlowski, J. Zdanowski, J. Grimblot, and J. Laureyns, Microstructural Transformations of TiO_2, Al_2O_3 + 13TiO_2 and Al_2O_3 + 40TiO_2 at Plasma Spraying and Laser Engraving, *Surf. Coat. Technol.*, 2004, **185**(2–3), p 137-149. https://doi.org/10.1016/j.surfcoat.2004.01.010
27. P. Baghery, M. Farzam, A.B. Mousavi, and M. Hosseini, Ni-TiO2 Nanocomposite Coating with High Resistance to Corrosion and Wear, *Surf. Coat. Technol.*, 2010, **204**(23), p 3804-3810. https://doi.org/10.1016/j.surfcoat.2010.04.061
28. J.J. Hao, Y.A. Bai, C.R. Wang, and X.Y. Liu, Fabrication and Characterization of Ni-TiO < Sub > 2</Sub > Nanocomposite Coatings and Their Corrosion Resistance Behaviors, *Mater. Sci. Forum*, 2011, **688**, p 217-222. https://doi.org/10.4028/www.scientific.net/MSF.688.217

29. S. Singh and M. Kaur, Mechanical and Microstructural Properties of NiCrFeSiBC/Cr_3C_2 Composite Coatings—Part I, *Surf. Eng.*, 2014, **32**, p 1-11
30. C.R.C. Lima and J.M. Guilemany, Adhesion Improvements of Thermal Barrier Coatings with HVOF Thermally Sprayed Bond Coats, *Surf. Coat. Technol.*, 2007, **201**(8), p 4694-4701
31. G. Sundararajan and P.G. Shewmon, A New Model for the Erosion of Metals at Normal Incidence, *Wear*, 1983, **84**(2), p 237-258. https://doi.org/10.1016/0043-1648(83)90266-1